Intermittency and non-universality of pair dispersion in isothermal compressible turbulence

Sadhitro De[1] †, Dhrubaditya Mitra[2] ‡, and Rahul Pandit[3] ¶

[1]Department of Physics, University of Oxford, Oxford, United Kingdom.

[2]Nordita, KTH Royal Institute of Technology and Stockholm University, Hannes Alfvens väg 12, 10691 Stockholm, Sweden.

[3]Department of Physics, Indian Institute of Science, Bangalore 560012, India.

(Received xx; revised xx; accepted xx)

Statistical properties of the pair dispersion of Lagrangian particles (tracers) in incompressible turbulent flows provide insights into transport and mixing. We explore the same in transonic to supersonic compressible turbulence of an isothermal ideal gas in two dimensions, driven by large-scale solenoidal and irrotational stirring forces, via direct numerical simulations. We find that the scaling exponents of the order-p negative moments of the distribution of exit times – in particular, the doubling and halving times of pair separations – are nonlinear functions of p. Furthermore, the doubling and halving time statistics are different. The halving-time exponents are universal – they satisfy their multifractal model-based prediction, irrespective of the nature of the stirring. However, the doubling-time exponents are not. In the solenoidally-stirred flows, the doubling time exponents can be expressed solely in terms of the multifractal scaling exponents obtained from the structure functions of the solenoidal component of the velocity. Moreover, they depend strongly on the Mach number, Ma, as elongated patches of high vorticity emerge along shock fronts at high Ma. In contrast, in the irrotationally-stirred flows, the doubling-time exponents do not satisfy any known multifractal model-based relation, and are independent of Ma. Our findings are of potential relevance to astrophysical disks and molecular clouds wherein turbulent transport and mixing of gases often govern chemical kinetics and the rates of formation of stars and planetesimals.

Key words: Compressible turbulence; Particle/Fluid Flow

1. Introduction

One of the pillars of our understanding of turbulence is the *Richardson's law* (Richardson 1926): $\left\langle R^2(t)\right\rangle \sim t^3$, where R is the separation between a pair of Lagrangian particles or tracers, t is the time, and $\langle\cdot\rangle$ denotes averaging over all tracer-pairs at the given instant t which belongs to the statistically stationary turbulent state. This law holds for incompressible flows

† Email address for correspondence: sadhitro.de@physics.ox.ac.uk
‡ Email address for correspondence: dhruba.mitra@gmail.com
¶ Email address for correspondence: rahul@iisc.ac.in

if R lies within the inertial range of length scales, across which the nonlinear interactions dominate over viscous dissipation. Here, we seek a generalization of Richardson's law to compressible turbulent flows, which are prevalent in many astrophysical systems (Mac Low & Klessen 2004; McKee & Ostriker 2007; Elmegreen & Scalo 2004).

We begin by summarizing the evidence in support of Richardson's law in incompressible turbulence. Theoretically, it can be understood as a modeling of the evolution of $R(t)$ by a diffusive process (Richardson 1926; Benzi & Toschi 2023) with a diffusion constant, $K(R) \sim R^{4/3}$, that stems (Benzi & Toschi 2023) from Kolmogorov's 1941 (K41) theory (Kolmogorov 1941). An alternative interpretation of Richardson's law is in terms of a dynamic scaling exponent, $z = 2/3$, such that typical time scales, $\tau(r)$, of turbulent eddies of size r scale as $\tau(r) \sim r^z$. It is now well established, from experiments and DNS, that K41 must be generalized to include intermittency, i.e., the p-th moment of the Eulerian velocity difference, δu, across a length scale r (the order-p velocity structure function), scales as $\langle \delta u^p(r) \rangle \sim r^{\zeta_p}$, where ζ_p is a nonlinear concave function of p (Frisch 1996). This also dictates that turbulence must, in fact, have an infinite number of dynamic exponents (L'vov *et al.* 1997; Mitra & Pandit 2004, 2005; Ray *et al.* 2008, 2011; Pandit *et al.* 2008), suggesting the presence of intermittency corrections to Richardson's law, which itself enjoys feeble support from experiments (Ott & Mann 2000; Shnapp *et al.* 2018; Elsinga *et al.* 2022; Tan & Ni 2022; Shnapp *et al.* 2023) and direct numerical simulations (DNS) (Salazar & Collins 2009; Bitane *et al.* 2012, 2013; Bragg *et al.* 2016; Buaria *et al.* 2015; Elsinga *et al.* 2022) – the observed scaling range of $\left\langle R^2 \right\rangle$ is at most a decade. A better approach to investigate the intermittency of pair dispersion in turbulence is to use *exit times*, defined as the time, $\tau_\alpha(R)$, it takes for R to cross αR *for the first time*, where α is fixed. The choice $\alpha > 1$ corresponds to the *doubling times*†, $\tau_{\rm D}$, for which (Boffetta *et al.* 1999; Boffetta & Sokolov 2002*a*,*b*)

$$\left\langle \tau_{\rm D}^{-p}(R) \right\rangle \sim R^{-\chi_{\rm p}^{\rm D}}, \quad \text{where} \quad \chi_{\rm p}^{\rm D} = p - \zeta_p \,. \tag{1.1}$$

This bridge relation between the dynamic exponents, $\chi_{\rm p}^{\rm D}$, and ζ_p has been obtained by using the multifractal model of turbulence (Parisi & Frisch 1985; Frisch 1996).

In compressible flows, in addition to doubling times, we need to define *halving times*, $\tau_{\rm H}(R)$, for which $\alpha < 1$ and the corresponding scaling exponents are $\chi_{\rm p}^{\rm H}$. As the multifractal model does not distinguish between the doubling and halving times, $\chi_{\rm p}^{\rm H}$ are also expected naively to satisfy the same bridge relation, (1.1). Although there have been many studies of the statistics of velocity increments in compressible turbulence (Boldyrev *et al.* 2002*b*,*a*; Schmidt *et al.* 2008; Konstandin *et al.* 2012; Wang *et al.* 2012*a*; Kritsuk *et al.* 2007; Wang *et al.* 2017; Jagannathan & Donzis 2016), none have investigated the intermittency of tracer pair dispersion. We explore this via simulations of forced compressible turbulence of an isothermal ideal gas, governed by the Navier-Stokes equations. We restrict ourselves to two spatial dimensions in order to reach high resolutions.

Two-dimensional (2D) incompressible turbulence is different from its 3D counterpart because, in addition to the kinetic energy, the enstrophy is conserved in the limit of zero viscosity and forcing. Theory, experiments and DNS indicate that $\left\langle R^2(t) \right\rangle$ grows exponentially with time in the direct–enstrophy–cascade regime (Bennett 1984; Rivera & Ecke 2005; Jullien 2003; LaCasce & Ohlmann 2003). In 2D *compressible* turbulence, there is small-scale dissipation of kinetic energy via acoustic waves (Falkovich & Kritsuk 2017). It has been shown that $\left\langle R^2(t) \right\rangle$ grows as a power–law beyond the dissipation scales in models of such flows, e.g., surface flows (Cressman & Goldburg 2003; Li *et al.* 2024) and the 2D Burgers equation (De *et al.* 2024).

† To be accurate, $\alpha = 2$ means "doubling". Nevertheless, in practice, any $\alpha > 1$ is used (Boffetta & Sokolov 2002*a*)

Here too, we unveil a power-law growth of $\left\langle R^2(t)\right\rangle$ across similar spatial scales. While, $\chi_{\rm p}^{\rm H}$ obey the multifractal model-based bridge relation and are universal, $\chi_{\rm p}^{\rm D} \neq \chi_{\rm p}^{\rm H}$, in disagreement with the multifractal model. If the external force is solenoidal: (a) $\chi_{\rm p}^{\rm D} = p - \zeta_p^{\rm s}$, where $\zeta_p^{\rm s}$ are the scaling exponents of *structure functions of the solenoidal component of the velocity field*; and (b) the values of $\chi_{\rm p}^{\rm D}$ (and consequently, $\zeta_p^{\rm s}$) depend on Ma. This indicates that vortical structures play the dominant role in pair dispersion, and we demonstrate that their fractal dimensions vary significantly with Ma, accounting for the Ma-dependence of $\chi_{\rm p}^{\rm D}$. If the force is purely irrotational, $\chi_{\rm p}^{\rm D}$ neither follows any known bridge relation, nor depends on Ma. In this case, the regions of large flow divergence affect pair dispersion.

In Section 2, we describe the model, and outline its parameters and the details of its DNS. In Section 3, we delineate our analyses of particle pair-dispersion and Lagrangian exit-times, and then provide the concluding remarks in Section 4.

2. Model and its numerical simulation

The equations (Haugen *et al.* 2022) governing the dynamics of a compressible isothermal ideal gas are:

$$\partial_t \rho + \partial_j(\rho u_j) = 0\,, \tag{2.1a}$$

$$\partial_t u_i + u_j\partial_j u_i = -\frac{1}{\rho}\partial_i P + \frac{1}{\rho}\partial_j(\nu\rho\sigma_{ij} + \rho\zeta_{\rm bulk}\delta_{ij}\partial_k u_k) + \mathcal{P}_{ij}(\xi) f_j\,, \tag{2.1b}$$

where $\boldsymbol{u}(\boldsymbol{x},t)$ is the velocity field, $\rho(\boldsymbol{x},t)$ is the density field, P is the pressure, ν is the kinematic shear viscosity, $\zeta_{\rm bulk}$ is the bulk viscosity, δ_{ij} is the Kronecker delta, $\mathcal{P}_{ij}(\xi) f_j$ is the external force, $\sigma_{ij} = (1/2)\left(\partial_j u_i + \partial_i u_j\right) - (1/2)\delta_{ij}\partial_k u_k$ is the traceless rate-of-strain tensor, and the equation of state is given by $P = c_{\rm s}^2\rho$, where $c_{\rm s}$ is the (constant) speed of sound. The quantity, $\boldsymbol{f}$, which we call external force or stirring, is white-in-time and its Fourier transform has compact support at $|\boldsymbol{k}| = k_{\rm f} = 3$, where $\boldsymbol{k}$ is the wave vector. The Fourier transform of the projection operator, $\mathcal{P}_{ij}(\xi)$ is, $\hat{\mathcal{P}}_{ij}(\xi) \equiv \xi\delta_{ij} + (1-2\xi)k_i k_j/k^2$. We consider two cases, $\xi = 0$ and 1, which correspond, respectively, to an irrotational and a solenoidal external force (see Table 1). The assumption of isothermality holds when the medium is optically thin (transparent to radiation) in which case the heat generated by dissipation at shocks is rapidly radiated away. This is generally valid for molecular clouds which have low density and solar metallicity (Mac Low & Klessen 2004).

We perform pseudospectral DNS of Eq. (2.1) on a 2D doubly-periodic square domain of side $L = 2\pi$ with $N^2 = 4096^2$ collocation points. The bulk viscosity follows the prescription outlined by Von Neumann & Richtmyer (1950): it is zero everywhere except near the shocks. We assume ν to be a constant. This is a common practice; see, e.g., Haugen *et al.* (2022); Federrath *et al.* (2011); Richard *et al.* (2022). After the flow reaches a statistically stationary state we seed it uniformly with $n = N^2$ Lagrangian particles or tracers at every grid point, such that the distance between a pair of nearest-neighbor tracers is the grid spacing. The position of the m-th tracer, $\boldsymbol{X}^{\rm m}(t)$, evolves according to

$$\frac{d\boldsymbol{X}^{\rm m}(t)}{dt} = \boldsymbol{V}^{\rm m}(t) \quad \text{where} \quad \boldsymbol{V}^{\rm m}(t) = \boldsymbol{u}(\boldsymbol{x},t)\delta(\boldsymbol{x} - \boldsymbol{X}^{\rm m}). \tag{2.2}$$

They cluster at the shocks and their number density maps $\rho(\boldsymbol{x},t)$.

The Reynolds and turbulent Mach numbers are defined, respectively, as ${\rm Re} \equiv u_{\rm rms}L/\nu$ and ${\rm Ma} \equiv u_{\rm rms}/c_{\rm s}$, where $u_{\rm rms}$ is the root-mean-square velocity. Using Helmholtz decomposition, we write $\boldsymbol{u} = \boldsymbol{u}^{\rm s} + \boldsymbol{u}^{\rm c}$, where $\boldsymbol{u}^{\rm s}$ and $\boldsymbol{u}^{\rm c}$ are, respectively, the solenoidal ($\boldsymbol{\nabla}\cdot\boldsymbol{u}^{\rm s} = 0$) and irrotational ($\boldsymbol{\nabla}\times\boldsymbol{u}^{\rm c} = 0$) components of the flow. The relative importance of $\boldsymbol{u}^{\rm s}$ and $\boldsymbol{u}^{\rm c}$ in

Run	ξ	c_s	u_{rms}	Ma	Re	L_I	T_E	Ψ	ϵ	λ	Re_λ	η
S1	1	0.05	0.053	1.05	6.7×10^3	1.66	32	0.82	8.1×10^{-6}	0.29	306	0.0111
S2	1	0.02	0.050	2.5	6.3×10^3	1.20	24	0.68	9.6×10^{-6}	0.26	255	0.0107
C1	0	0.05	0.038	0.75	4.7×10^3	1.04	28	0.19	1.3×10^{-5}	0.16	123	0.0099
C2	0	0.02	0.040	2.0	5.0×10^3	1.17	29	0.34	8.7×10^{-6}	0.21	172	0.0109

Table 1: **Simulation parameters.** Runs S1 and S2 have a solenoidal external force whereas C1 and C2 have an irrotational force. The parameters are defined as follows: c_s is the speed of sound, u_{rms} is the root-mean-square velocity, Ma is the Mach number, Re = $(u_{rms}L/\nu)$ is the box-size Reynolds number, $E(k)$ is the kinetic energy spectrum, $L_I = \pi \sum_k [E(k)/k] \Big/ \sum_k E(k)$ is the integral length scale, $T_E = L_I/u_{rms}$ is the large-eddy turnover time, Ψ is the solenoidal ratio defined in (2.3), $\epsilon = \left\langle \nu\rho\sigma_{ij}\partial_j u_i \right\rangle \Big/ \langle\rho\rangle$ is the rate of dissipation of kinetic energy per unit mass, $\lambda = \sqrt{5\nu u_{rms}^2 \Big/ \epsilon}$ is the Taylor microscale, $Re_\lambda = u_{rms}\lambda/\nu$ is the Taylor-microscale Reynolds number, and $\eta = \left(\nu^3/\epsilon\right)^{1/4}$ is the dissipation scale. In all the runs, $\nu = 5\times10^{-5}$ and number of tracers is $n = 4096^2$. Note that the length scales in this Table are not normalized by $L = 2\pi$.

the total kinetic energy is measured by the *solenoidal ratio*,

$$\Psi \equiv \frac{\left\langle \rho |\boldsymbol{u}^s|^2 \right\rangle}{\left\langle \rho |\boldsymbol{u}|^2 \right\rangle}, \tag{2.3}$$

which is the ratio of the total kinetic energy in the solenoidal modes to the total kinetic energy. All these parameters of our DNS are summarized in Table 1. We use L as our unit of length, and T_E, the large-eddy turnover time, as our unit of time. Further details about the DNS are given in Appendix A.

3. Results

We perform four sets of DNSs, two for $\xi = 1$, S1 and S2, and two for $\xi = 0$, C1 and C2. Typically, subsonic and supersonic compressible flow can be qualitatively different. Hence we perform a set of simulations that are transonic, Runs S1 and C1, Ma $\simeq$ 1, and another set S2 and C2 that are supersonic, Ma $>$ 1. In Fig. 1 we show pseudocolour plots of $\boldsymbol{\nabla}\cdot\boldsymbol{u}$, $\boldsymbol{\omega} = \boldsymbol{\nabla}\times\boldsymbol{u}$, and $\log_{10}\rho$ for all the cases or runs. The shocks are clearly visible as filamentary structures with large negative values of $\boldsymbol{\nabla}\cdot\boldsymbol{u}$. Naively, we may expect that the presence of the shocks would not show up in pseudocolour plot of $\boldsymbol{\omega}$, but this not the case – the shocks can be seen as almost one-dimensional manifolds with large absolute values of the vorticity: This is because, although a shock front that is a straight line does not contribute to vorticity, *curved* shock fronts do. In our simulations, (a) the density fluctuations are larger for the supersonic cases compared to the transonic ones and (b) the vorticity is more uniformly distributed in the transonic cases than the supersonic ones, for a given type of external forcing, as observed in Fig. 1.

In compressible turbulence, we can define p-th order longitudinal structures functions of

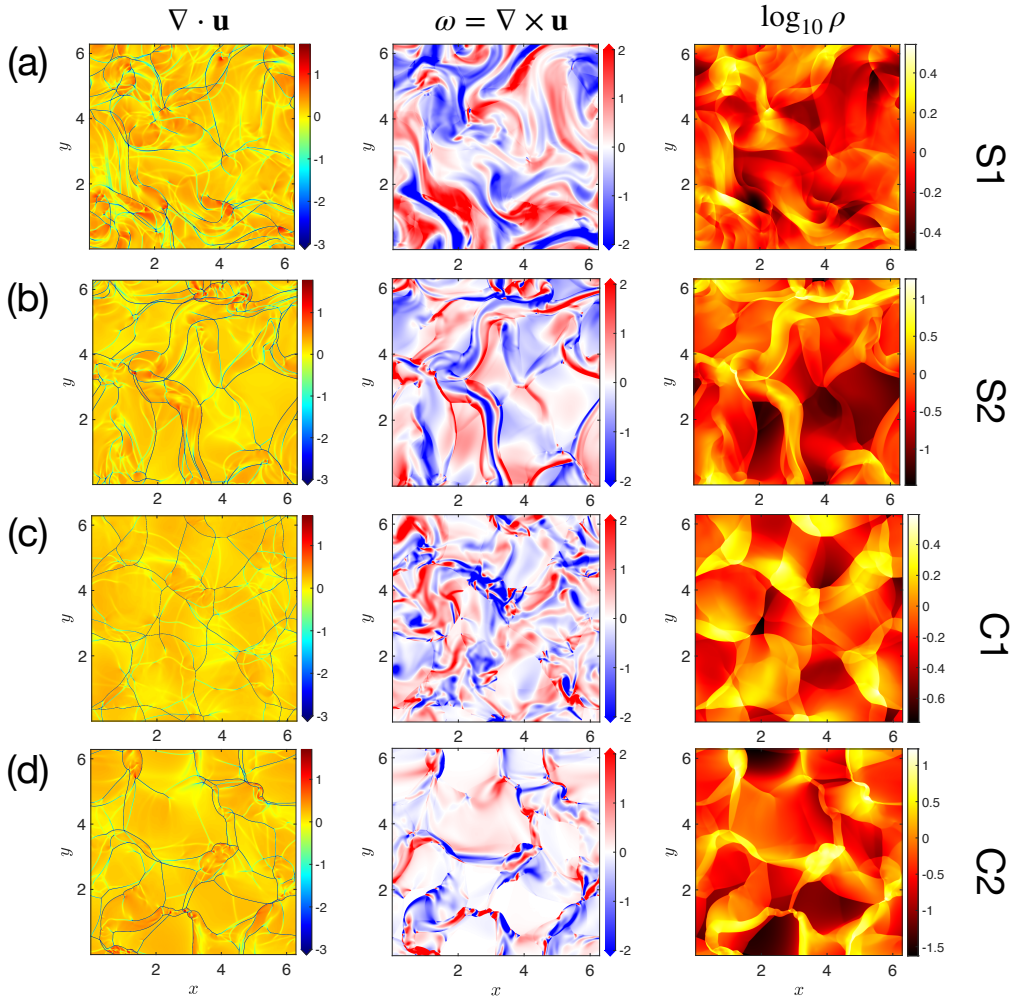

Figure 1: **Typical snapshots** of $\nabla \cdot \mathbf{u}$, vorticity $\boldsymbol{\omega} = \hat{z} \cdot \boldsymbol{\nabla} \times \boldsymbol{u}$, and $\log_{10} \rho$, in the cases (a) S1, (b) S2, (c) C1 and (d) C2. In each plot, $\boldsymbol{\nabla} \cdot \boldsymbol{u}$ and $\boldsymbol{\omega}$ are normalized by their respective root-mean-square (rms) values. Shocks are clearly visible in the $\boldsymbol{\nabla} \cdot \boldsymbol{u}$ profiles as the blue filament–like structures. The vorticity field, ω, is smoother in S1 than in S2 which contains nearly one-dimensional structures of intense vorticity bordering the shocks; in all figures, the areas of high vorticity lie in the vicinity of shocks. Similarly the spatial distribution of ω is more homogeneous in C1 than in C2. The values of ρ are clearly enhanced near the shocks; for a given type of external forcing, ρ tends to take much higher values at higher Mach numbers, Ma.

$\boldsymbol{u}$ as well as its components, $\boldsymbol{u}^{\rm s}$ and $\boldsymbol{u}^{\rm c}$:

$$\delta u_{\parallel}(r) \equiv [\boldsymbol{u}(\boldsymbol{x}+\boldsymbol{r}) - \boldsymbol{u}(\boldsymbol{x})] \cdot \frac{\boldsymbol{r}}{r} \quad \text{and} \quad \delta u_{\parallel}^{\rm s,c}(r) \equiv [\boldsymbol{u}^{\rm s,c}(\boldsymbol{x}+\boldsymbol{r}) - \boldsymbol{u}^{\rm s,c}(\boldsymbol{x})] \cdot \frac{\boldsymbol{r}}{r}; \quad (3.1a)$$

$$\text{with} \quad S_{\rm p}(r) = \left\langle |\delta u(r)_{\parallel}|^p \right\rangle, \quad S_{\rm p}^{\rm s,c}(r) = \left\langle |\delta u(r)_{\parallel}^{\rm s,c}|^p \right\rangle, \quad (3.1b)$$

$$\text{and} \quad S_{\rm p}(r) \sim r^{\zeta_p}, \quad S_{\rm p}^{\rm s}(r) \sim r^{\zeta_p^{\rm s}}, \quad S_{\rm p}^{\rm c}(r) \sim r^{\zeta_p^{\rm c}}. \quad (3.1c)$$

The scaling relations hold for $\eta \ll r \ll L_{\rm I}$, where η is the dissipation scale and $L_{\rm I}$ is the integral scale. All the exponents, ζ_p, $\zeta_p^{\rm s}$ and $\zeta_p^{\rm c}$ are nonlinear monotone increasing functions of p (Konstandin *et al.* 2012; Wang *et al.* 2017, 2012*b*) (see Appendix B.2).

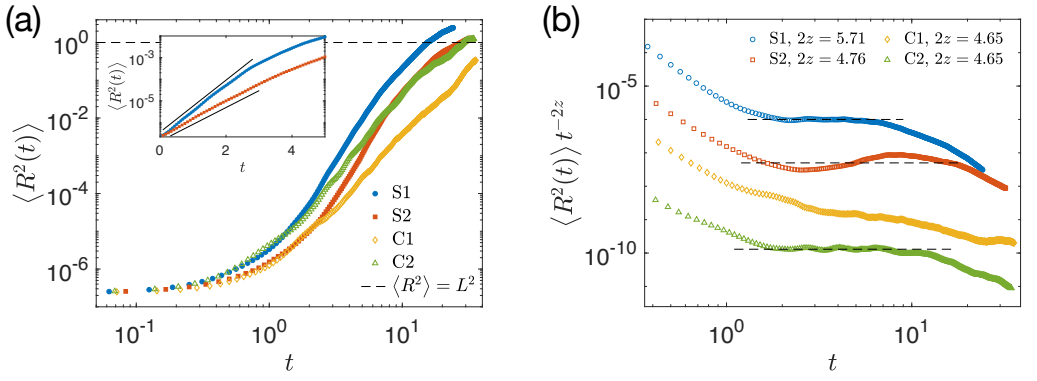

Figure 2: **Mean-squared separation.** (a) Log-log plots of the time evolution of the mean-squared separation, $\langle R^2(t) \rangle$, between two tracers. The growth of $\langle R^2 \rangle$ is faster in S1 than in S2, and faster in C2 than in C1. *Inset:* Semi-log graphs of $\langle R^2 \rangle$ for S1 and S2 displaying exponential growth at early times. (b) Log-log plots of $\langle R^2 \rangle$ compensated by $t^{2/z}$, where $z = 1 - \zeta_2/2$; power-law growth of $\langle R^2 \rangle$ across its inertial range values appears to occur in every run; in C1, $\langle R^2 \rangle$ clearly scales more slowly than $t^{2/z}$ in this range.

3.1. *Pair dispersion*

In order to study pair dispersion, we investigate how the separation, $R(t)$, between a pair of nearest-neighbor tracers, separated initially by the grid-spacing (approximately 0.3η), evolves with time. We calculate $\langle R^2(t) \rangle$ by averaging, at every instant, over the $2n$ separations. Our results are shown in Fig. (2a). At early times, $\langle R^2(t) \rangle$ grows exponentially for all the runs [For S1 and S2 we show the plots in the inset of Fig. (2a)]. This range of exponential growth is very small for C1 and C2. Similar results (Jullien 2003) have been obtained for incompressible 2D turbulence. Exponential growth up to a length scale typically implies that the flow across the tracers is smooth up to that scale. This holds for our simulations because at such small time scales most of the pair separations lie away from shocks. We note that at late times the behavior of $\langle R^2 \rangle$ is not universal, it depends on precisely how the DNS is forced.

If $R(t)$ lies in the inertial range, then $R^2 \sim t^{2/(1-h)}$, where h is the local Hölder exponent of the velocity fluctuations in space. If we use Kolmogorov's simple scaling hypothesis, $\zeta_2 = 2h$ which yields $\langle R^2(t) \rangle \sim t^{2/z}$, where $z = 1 - \zeta_2/2$. In incompressible flows, $\zeta_2 = 2/3$ and $z = 2/3$, which corresponds to Richardson scaling. For our simulations, in each case, we calculate ζ_2 from the scaling of the second order structure functions, $S_2(r)$. In Fig. (2b), we display the plots of $\langle R^2 \rangle$ compensated by $t^{2/z}$. It appears that there is a range of scales over which $\langle R^2 \rangle \sim t^{2/z}$ in S1, S2 and C2, while the increase in $\langle R^2(t) \rangle$ in C1 is visibly slower that $t^{2/z}$. However, in every case, the scaling regime is too small to make robust quantitative measurements of the values of z from the $\langle R^2(t) \rangle$ versus t plots. Hence, we turn to exit-times.

3.2. *Exit times*

To study the exit-time statistics, we now consider only those tracer pairs whose initial separations, R, belong to the inertial range, i.e., $\eta \ll R \ll L_I$. Given the periodic boundary conditions, there are $2n$ distinct separations for any R. As the tracers evolve with the flow, we calculate the first instances of time at which R decreases below $3R/4$ or exceeds $3R/2$, denoting them as *halving times*, $\tau_H(R)$, and *doubling times*, $\tau_D(R)$, respectively. We consider 25 different values of R, see Appendix C. The statistics of exit times is expected to reveal the dynamic multiscaling exponents if the distances R, $3R/2$ and $3R/4$ lie within the inertial range. As long as this condition is satisfied, we expect our results to be independent of

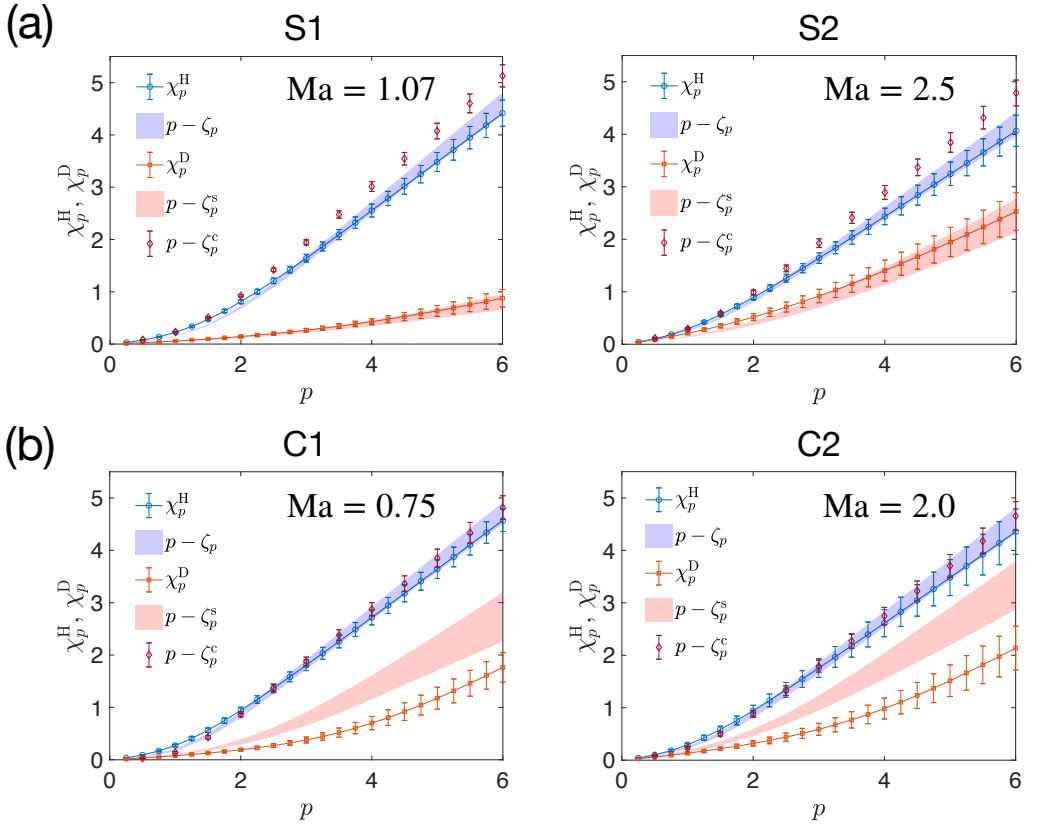

Figure 3: **Dynamic exponents** for doubling and halving times (see text) $\chi_{\rm p}^{\rm D}$ and $\chi_{\rm p}^{\rm H}$, respectively, as functions of the order p which takes integer and fractional values up to 6. The blue shaded region corresponds to the bridge relation, $p-\zeta_p$, derived from the multifractal model. The pink shaded region corresponds to the expression $p-\zeta_p^{\rm s}$.

the particular choice of the thresholds, $3R/2$ or $3R/4$. Crucially, over the inertial range, the equal–time structure functions $S_{\rm p}(r)$, $S_{\rm p}^{\rm s}(r)$ and $S_{\rm p}^{\rm c}(r)$ [see (3.1)] show scaling; see Appendix B.2. For each R, we calculate the moments $\left\langle \tau_{\rm H}^{-p}(R)\right\rangle$ and $\left\langle \tau_{\rm D}^{-p}(R)\right\rangle$ over three large-eddy-turnover-time. The averaging is over all $2n$ pairs with the same value of R. We find that these moments scale with R as,

$$\left\langle \tau_{\rm D}^{-p}(R)\right\rangle \sim R^{-\chi_{\rm p}^{\rm D}} \quad \text{and} \quad \left\langle \tau_{\rm H}^{-p}(R)\right\rangle \sim R^{-\chi_{\rm p}^{\rm H}}, \tag{3.2}$$

in the all cases (see Appendix C). Note that the scaling ranges in the different cases are slightly different as they depends on how the flow is stirred. However, in every run, they extend more than a decade in R for all p. Moreover, their range of scaling overlaps with with those of the equal-time structure functions (3.1).

We extract the exponents, $\chi_{\rm p}^{\rm D}$, $\chi_{\rm p}^{\rm H}$, ζ_p, $\zeta_p^{\rm c}$ and $\zeta_p^{\rm s}$, by linear least–square fitting of the log-log plots of $\left\langle \tau_{\rm D}^{-p}(R)\right\rangle$, $\left\langle \tau_{\rm H}^{-p}(R)\right\rangle$, $S_{\rm p}(r)$, $S_{\rm p}^{\rm s}(r)$ and $S_{\rm p}^{\rm c}(r)$, respectively. We repeat the above procedure for an ensemble of $M = 10$ snapshots in the statistically stationary state. For each exponent, its final value is its ensemble mean, and its error bars are defined by the standard deviation. In Fig. (3) we plot the dynamic exponents, $\chi_{\rm p}^{\rm D}$ and $\chi_{\rm p}^{\rm H}$, for all the runs, up to $p = 6$. Both are nonlinear functions of p, indicating *dynamic multiscaling*. The spreads of the shaded regions in Fig. 3 show the error bars of the dynamic scaling exponents.

The multifractal model (Parisi & Frisch 1985; Frisch 1996) does not distinguish between doubling and halving times, and hence, for both of them it predicts the bridge relation, $\chi_{\rm p}^{\rm H,D} = p - \zeta_p$. Our data for the halving–time exponents $\chi_{\rm p}^{\rm H}$ agree well with this in all the runs (see Fig. 3). However, we find unambiguously that $\chi_{\rm p}^{\rm D} \neq \chi_{\rm p}^{\rm H}$, thereby violating the simple expectation based on the multifractal model.

For the two runs with a solenoidal external force, S1 and S2, we find $\chi_{\rm p}^{\rm D} = p - \zeta_p^{\rm s}$, i.e., the bridge relation from the multifractal model holds for the doubling-time exponents, but with ζ_p replaced by $\zeta_p^{\rm s}$. Together this demonstrates that for the runs S1 and S2: the solenoidal part of the velocity field is primarily responsible for doubling, but both the solenoidal and irrotational parts affect halving. Note that the bridge relations hold for the two values of Ma we have used although the precise values of the exponents themselves depend on Ma.

For the two irrotationally-forced runs, C1 and C2, besides $\chi_{\rm p}^{\rm H} = p - \zeta_p$, we find that the relation $\chi_{\rm p}^{\rm H} = p - \zeta_p^{\rm c}$ also holds because the scaling exponents, $\zeta_p^{\rm c}$, of the irrotational component of the velocity are quite close to ζ_p. Crucially, $\chi_{\rm p}^{\rm D} \neq \chi_{\rm p}^{\rm H}$ again. Furthermore, unlike the runs S1 and S2, $\chi_{\rm p}^{\rm D} \neq p - \zeta_p^{\rm s}$ [see Fig. (3)]. This indicates that the growth of R is not determined solely by the solenoidal part of the velocity field, but is affected significantly by the regions of the flows with $\boldsymbol{\nabla} \cdot \boldsymbol{u} > 0$. A quantitative understanding of these exponents remains an open question. Finally, given the accuracy of our data, we do not detect any dependence of these exponents on Ma.

Let us now try to identify the structures in the flow that are primarily responsible for the observed scaling by using the multifractal model. We consider the velocity field to comprise an infinity of interwoven sets, $\mathcal{S}_{\rm h}$, each characterized by a scaling exponent, h, and fractal dimension, $D(h)$. For any point $\boldsymbol{x} \in \mathcal{S}_{\rm h}$, $\delta u_\parallel(R) \sim R^h$, in the limit $R/L_{\rm I} \to 0$. We use this model to calculate the dynamic exponents, $\chi_{\rm p}$. The characteristic time scale (here, exit time), $\tau_{\boldsymbol{x}}(R) \sim R/[\delta u_\parallel(R)] \sim R^{1-h}$. Its moments of negative orders, $-p$ ($p > 0$), scale as

$$\langle \tau^{-p}(R) \rangle \sim \int dw(h) \left(\frac{R}{L_{\rm I}}\right)^{-p(1-h)} \left(\frac{R}{L_{\rm I}}\right)^{d-D(h)} \sim R^{-\chi_{\rm p}}\,; \tag{3.3a}$$

$$\implies -\chi_{\rm p} = \inf_h \left[ph + d - p - D(h)\right] \quad \text{and} \quad D(h) = \inf_p \left(ph + d - p + \chi_{\rm p}\right)\,. \tag{3.3b}$$

The spatial dimensionality $d = 2$, and $dw(h)$ gives the weights of the different exponents. For $R/L_{\rm I} \to 0$, the integral in (3.3a) is evaluated by the method of steepest descents. Equation (3.3b) implies that $D(h)$ and $\chi_{\rm p}$ are Legendre transforms of each other. Physically, $D(h)$ reveals the dimensionality of structures that contribute to the scaling of $\delta u_\parallel(R)$ with the exponent h, unveiling the *multifractal spectrum*. Note that, even if $D(h)$ is not concave its Legendre transform $\chi_{\rm p}$ will be concave; however, the inverse transform returns not $D(h)$ but its concave hull (see, e.g., Frisch 1996, section 8.5).

Here, we define $D_{\rm H}(h)$ and $D_{\rm D}(h)$, which are calculated from $\chi_{\rm p}^{\rm H}$ and $\chi_{\rm p}^{\rm D}$, respectively, by using Eq. (3.3b). Displayed in Fig. (4), they clearly show that the halving and doubling times are influenced by different structures. In Fig. 4(a), we note that changes in the type of external force and Ma have very little effect on $D_{\rm H}(h)$. In all cases, it goes down to unity as $h \to 0$. Thus, it is reasonable to conclude that the halving times are affected by shocks, which are one-dimensional structures characterized by $h \to 0$. Since $\chi_{\rm p}^{\rm H} = p - \zeta_p$, $D_{\rm H}(h)$ overlaps with the multifractal spectrum evaluated from ζ_p. The dependence of $D_{\rm D}(h)$ on Ma in S1 and S2 is much stronger, as shown in Fig. (4b). In S1 (Ma $\simeq$ 1), $D_{\rm D}(h)$ does not go down to 1, implying that the structures that influence the increase of $R(t)$ are more space-filling than shocks. In S2 (Ma $\simeq$ 2.5), $D_{\rm D}(h)$ does decrease to unity indicating that nearly one-dimensional structures mediate the fast growth of R. Since $h \simeq 0.4 > 0$ when

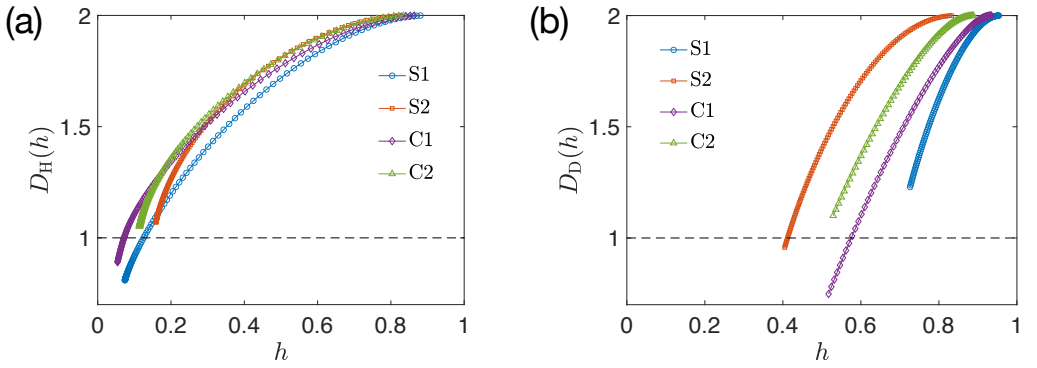

Figure 4: **D(h) vs h**. Plots of (a) $D_{\rm H}(h)$ and (b) $D_{\rm D}(h)$ versus h for all the runs. $D_{\rm H}(h)$ changes slightly as we change the type of external force and Ma; the dependence of $D_{\rm D}(h)$ on Ma is much stronger in case of the solenoidal external force than the irrotational one. For S2, C1 and C2, $D_{\rm D}(h)$ takes values close to unity but not S1, implying that 1D structures contribute to the scaling of the doubling times in the former cases.

$D_{\rm D}(h) \simeq 1$ and $\chi^{\rm D}_{\rm p} = p - \zeta^{\rm s}_p$, we infer that these structures are the thin elongated patches of high vorticity, which appear in the vicinity of the shocks, clearly visible in Fig.1. Such patches do exist for S1, but they are relatively weaker and broader. Finally, we note from Fig. (4b) that the function $D_{\rm D}(h)$ takes values close to unity in the runs, C1 and C2, as well. The development of a quantitative understanding of the exponents, $\chi^{\rm D}_{\rm p}$, in these runs remains a challenge.

4. Conclusion and Discussions

We have thus obtained insights into the multifractal nature of tracer pair dispersion in transonic to supersonic compressible turbulence of an isothermal ideal gas in 2D. The *doubling* and *halving* times of pair separations robustly quantify this intermittency and multifractality. Their statistics are different from each other, and the scaling exponents of the moments of their distributions, $\chi^{\rm D}_{\rm p}$ and $\chi^{\rm H}_{\rm p}$, vary nonlinearly with p. Therefore, these exit times encapsulate the dynamic multiscaling properties of compressible turbulence. While $\chi^{\rm H}_{\rm p}$ satisfies its multifractal model-based bridge relation and is universal, $\chi^{\rm D}_{\rm p}$ is not, depending on both the external force and the turbulent Mach number, Ma. This non-universality of the inertial-range pair-dispersion statistics is remarkable, given that the inertial-range fluctuations are supposed to be independent of the external force. In the solenoidally-stirred flows, $\chi^{\rm D}_{\rm p}$ is expressible solely in terms of the scaling exponents of the solenoidal velocity fluctuations, implying that predominantly vortical structures influence the fast growth of pair separations. We show that their fractal dimensions vary considerably with Ma which explains the Ma-dependence of $\chi^{\rm D}_{\rm p}$. In contrast, in the irrotationally–stirred flows, pair dispersion is significantly accelerated by the positive flow divergences and $\chi^{\rm D}_{\rm p}$ does not depend on Ma – its comprehensive understanding remains an open problem, whose solution may require that we go beyond the multifractal model.

Note that we have previously undertaken similar studies in simpler models of compressible turbulence – the randomly-forced 1D (De *et al.* 2023) and 2D (De *et al.* 2024) Burgers equation. They have a few qualitative similarities with the results here – evidence of dynamic multiscaling and $\chi^{\rm D}_{\rm p} \neq \chi^{\rm H}_{\rm p}$. However, the Burgers equation assumes certain unphysical simplifications: (a) zero pressure (tracers remain trapped on shocks forever), (b) zero vorticity at all times, and (c) bifractal velocity fluctuations – which the model used here does not; thereby displaying richer, more realistic and more complicated features. This additional

complexity also precludes the formulation of a heuristic theoretical framework for the exit times which was possible in De *et al.* (2024).

We expect the key qualitative content of our results to be valid in three dimensions (3D) as well, although 3D, high-Ma compressible turbulence is different from its 2D counterpart. In particular, the robustness and indispensability of the two kinds of exit times in the exploration of the intermittency of pair dispersion, and the nature of their dependence on Ma and the external force, should carry over to 3D. Highly supersonic turbulent flows often govern various astrophysical processes, e.g. star formation in molecular clouds, and the transport and mixing of gases along with their chemical kinetics in the interstellar media (Mac Low & Klessen 2004; Elmegreen & Scalo 2004). Our work sets out an effective paradigm which can potentially provide in-depth insights into these aspects.

Acknowledgements. DM and RP would like to thank the Isaac Newton Institute for Mathematical Sciences, Cambridge, for support and hospitality during the programme Anti-diffusive dynamics: from sub-cellular to astrophysical scales, where partial work on this paper was undertaken. This work was supported by EPSRC grant EP/R014604/1.

Funding. DM acknowledges the support of the Swedish Research Council Grant No. 638-2013-9243. Nordita is partially supported by NordForsk. S.D. thanks the PMRF (India) for support. R.P. and S.D. thank the Science and Engineering Research Board (SERB), Anusandhan National Research Foundation (ANRF) and the National Supercomputing Mission (NSM), India for support, and the Supercomputer Education and Research Centre (IISc) for computational resources.

Declaration of interests. The authors report no conflict of interest.

Data availability statement. The data that support the findings of this study are available from the corresponding author upon request.

Author ORCIDs. S. De: https://orcid.org/0000-0002-1020-968X ; D. Mitra: https://orcid.org/0000-0003-4861-8152 ; R. Pandit: https://orcid.org/0000-0003-0948-8834

REFERENCES

Bennett, A. F. 1984 Relative dispersion: Local and nonlocal dynamics. *Journal of Atmospheric Sciences* **41** (11), 1881 – 1886.

Benzi, Roberto & Toschi, Federico 2023 Lectures on turbulence. *Physics Reports* **1021**, 1–106.

Bitane, Rehab, Homann, Holger & Bec, Jérémie 2012 Time scales of turbulent relative dispersion. *Physical Review E* **86** (4), 045302.

Bitane, Rehab, Homann, Holger & Bec, Jérémie 2013 Geometry and violent events in turbulent pair dispersion. *Journal of Turbulence* **14** (2), 23–45.

Boffetta, G., Celani, A., Crisanti, A. & Vulpiani, A. 1999 Pair dispersion in synthetic fully developed turbulence. *Phys. Rev. E* **60**, 6734–6741.

Boffetta, G. & Sokolov, I. M. 2002*a* Relative dispersion in fully developed turbulence: The richardson's law and intermittency corrections. *Phys. Rev. Lett.* **88**, 094501.

Boffetta, G. & Sokolov, I. M. 2002*b* Statistics of two-particle dispersion in two-dimensional turbulence. *Physics of Fluids* **14** (9), 3224–3232.

Boldyrev, Stanislav, Nordlund, Åke & Padoan, Paolo 2002*a* Scaling Relations of Supersonic Turbulence in Star-forming Molecular Clouds. *Astrophys. J.* **573** (2), 678–684.

Boldyrev, Stanislav, Nordlund, Åke & Padoan, Paolo 2002*b* Supersonic turbulence and structure of interstellar molecular clouds. *Phys. Rev. Lett.* **89**, 031102.

Bragg, Andrew D, Ireland, Peter J & Collins, Lance R 2016 Forward and backward in time dispersion of fluid and inertial particles in isotropic turbulence. *Physics of Fluids* **28** (1).

Breiman, Leo 1996 Bagging predictors. *Machine learning* **24**, 123–140.

Buaria, Dhawal, Sawford, Brian L & Yeung, Pui-Kuen 2015 Characteristics of backward and forward two-particle relative dispersion in turbulence at different reynolds numbers. *Physics of Fluids* **27** (10).

Canuto, Claudio, Hussaini, M Yousuff, Quarteroni, Alfio & Zang, Thomas A 2007 *Spectral methods: fundamentals in single domains*. Springer Science & Business Media.

Cressman, J. R. & Goldburg, W. I. 2003 Compressible flow: Turbulence at the surface. *J. Stat. Phys.* **113**, 875.

De, S., Mitra, D. & Pandit, R. 2023 Dynamic multiscaling in stochastically forced burgers turbulence. *Sci. Rep.* **13**, 7151.

De, Sadhitro, Mitra, Dhrubaditya & Pandit, Rahul 2024 Uncovering the multifractality of lagrangian pair dispersion in shock-dominated turbulence. *Phys. Rev. Res.* **6**, L022032.

Elmegreen, Bruce G. & Scalo, John 2004 Interstellar turbulence i: Observations and processes. *Annual Review of Astronomy and Astrophysics* **42**, 211–273.

Elsinga, GE, Ishihara, T & Hunt, JCR 2022 Non-local dispersion and the reassessment of richardson's t3-scaling law. *Journal of Fluid Mechanics* **932**, A17.

Falkovich, Gregory & Kritsuk, Alexei G. 2017 How vortices and shocks provide for a flux loop in two-dimensional compressible turbulence. *Phys. Rev. Fluids* **2**, 092603.

Federrath, C., Chabrier, G., Schober, J., Banerjee, R., Klessen, R. S. & Schleicher, D. R. G. 2011 Mach number dependence of turbulent magnetic field amplification: Solenoidal versus compressive flows. *Phys. Rev. Lett.* **107**, 114504.

Frisch, U. 1996 *Turbulence: The Legacy of A.N. Kolmogorov*. Cambridge University Press, Cambridge, England.

Haugen, Nils E. L., Brandenburg, Axel, Sandin, Christer & Mattsson, Lars 2022 Spectral characterisation of inertial particle clustering in turbulence. *J. Fluid Mech.* **934**, A37.

Higham, Desmond J 2001 An algorithmic introduction to numerical simulation of stochastic differential equations. *SIAM review* **43** (3), 525–546.

Hou, Thomas Y. & Li, Ruo 2007 Computing nearly singular solutions using pseudo-spectral methods. *Journal of Computational Physics* **226** (1), 379–397.

Jagannathan, Shriram & Donzis, Diego A 2016 Reynolds and mach number scaling in solenoidally-forced compressible turbulence using high-resolution direct numerical simulations. *Journal of Fluid Mechanics* **789**, 669–707.

Jullien, Marie-Caroline 2003 Dispersion of passive tracers in the direct enstrophy cascade: Experimental observations. *Physics of Fluids* **15** (8), 2228–2237, arXiv: https://pubs.aip.org/aip/pof/article-pdf/15/8/2228/19291870/2228_1_online.pdf.

Kolmogorov, A. N. 1941 On the degeneration of isotropic turbulence in an incompressible viscous fluids. *Dokl. Akad. Nauk. SSSR* **31**, 5385–541.

Konstandin, Lukas, Federrath, Christoph, Klessen, Ralf S. & Schmidt, Wolfram 2012 Statistical properties of supersonic turbulence in the Lagrangian and Eulerian frameworks. *J. Fluid Mech.* **692**, 183.

Kritsuk, Alexei G., Norman, Michael L., Padoan, Paolo & Wagner, Rick 2007 The statistics of supersonic isothermal turbulence. *The Astrophysical Journal* **665** (1), 416.

LaCasce, J. H. & Ohlmann, Carter 2003 Relative dispersion at the surface of the gulf of mexico. *Journal of Marine Research* **61** (3).

Li, Yaxing, Wang, Yifan, Qi, Yinghe & Coletti, Filippo 2024 Relative dispersion in free-surface turbulence. *Journal of Fluid Mechanics* **993**, R2.

L'vov, Victor S, Podivilov, Evgenii & Procaccia, Itamar 1997 Temporal multiscaling in hydrodynamic turbulence. *Physical Review E* **55** (6), 7030.

Mac Low, Mordecai-Mark & Klessen, Ralf S. 2004 Control of star formation by supersonic turbulence. *Rev. Mod. Phys.* **76**, 125–194.

McKee, Christopher F. & Ostriker, Eve C. 2007 Theory of star formation. *Annual Review of Astronomy and Astrophysics* **45**, 565–687.

Mehta, Pankaj, Bukov, Marin, Wang, Ching-Hao, Day, Alexandre GR, Richardson, Clint, Fisher, Charles K & Schwab, David J 2019 A high-bias, low-variance introduction to machine learning for physicists. *Physics reports* **810**, 1–124.

Mitra, Dhrubaditya & Pandit, Rahul 2004 Varieties of Dynamic Multiscaling in Fluid Turbulence. *Phys. Rev. Lett.* **93**, 024501.

Mitra, Dhrubaditya & Pandit, Rahul 2005 Dynamics of passive-scalar turbulence. *Phys. Rev. Lett.* **95** (14), 144501.

Ott, Søren & Mann, Jakob 2000 An experimental investigation of the relative diffusion of particle pairs in three-dimensional turbulent flow. *Journal of Fluid Mechanics* **422**, 207–223.

Pandit, R., Ray, S.S. & Mitra, D. 2008 Dynamic multiscaling in turbulence. *Eur. Phys. J. B* **64**, 463.

Parisi, Giorgio & Frisch, Uriel 1985 On the singularity structure of fully developed turbulence. *Turbulence*

and predictability in geophysical fluid dynamics and climate dynamics, Varenna, 1983, M. Ghil, R. Benzi and G. Parisi, eds. Proceedings of the International School of Physic Enrico Fermi, North-Holland 1985 pp. 84–88.

Ray, S. S., Mitra, D. & Pandit, R. 2008 The universality of dynamic multiscaling in homogeneous, isotropic Navier–Stokes and passive-scalar turbulence. *New J. Phys.* **10**, 033003.

Ray, Samriddhi Sankar, Mitra, Dhrubaditya, Perlekar, Prasad & Pandit, Rahul 2011 Dynamic Multiscaling in Two-Dimensional Fluid Turbulence. *Phys. Rev. Lett.* **107**, 184503.

Richard, Thibaud, Lesaffre, Pierre, Falgarone, Edith & Lehmann, Andrew 2022 Probing the nature of dissipation in compressible mhd turbulence. *Astron. Astrophys.* **664**, A193.

Richardson, Lewis Fry 1926 Atmospheric diffusion shown on a distance-neighbour graph. *Proceedings of the Royal Society of London. Series A, Containing Papers of a Mathematical and Physical Character* **110** (756), 709–737.

Rivera, M. K. & Ecke, R. E. 2005 Pair dispersion and doubling time statistics in two-dimensional turbulence. *Phys. Rev. Lett.* **95**, 194503.

Salazar, Juan PLC & Collins, Lance R 2009 Two-particle dispersion in isotropic turbulent flows. *Annual review of fluid mechanics* **41**, 405–432.

Schmidt, Wolfram, Federrath, Christoph & Klessen, Ralf 2008 Is the scaling of supersonic turbulence universal? *Phys. Rev. Lett.* **101**, 194505.

Schumacher, Jörg, Sreenivasan, Katepalli R & Yakhot, Victor 2007 Asymptotic exponents from low-reynolds-number flows. *New Journal of Physics* **9** (4), 89.

Shnapp, Ron, Brizzolara, Stefano, Neamtu-Halic, Marius M, Gambino, Alessandro & Holzner, Markus 2023 Universal alignment in turbulent pair dispersion. *Nature Communications* **14** (1), 4195.

Shnapp, Ron, Liberzon, Alex & others 2018 Generalization of turbulent pair dispersion to large initial separations. *Physical Review Letters* **120** (24), 244502.

Tan, Shiyong & Ni, Rui 2022 Universality and intermittency of pair dispersion in turbulence. *Phys. Rev. Lett.* **128**, 114502.

Von Neumann, J & Richtmyer, R D 1950 A method for the numerical calculation of hydrodynamic shocks. *Journal of applied physics* **21** (3), 232–237.

Wang, Jianchun, Gotoh, Toshiyuki & Watanabe, Takeshi 2017 Scaling and intermittency in compressible isotropic turbulence. *Phys. Rev. Fluids* **2**, 053401.

Wang, Jianchun, Shi, Yipeng, Wang, Lian-Ping, Xiao, Zuoli, He, X. T. & Chen, Shiyi 2012*a* Scaling and Statistics in Three-Dimensional Compressible Turbulence. *Phys. Rev. Lett.* **108**, 214505.

Wang, Jianchun, Shi, Yipeng, Wang, Lian-Ping, Xiao, Zuoli, He, X. T. & Chen, Shiyi 2012*b* Scaling and statistics in three-dimensional compressible turbulence. *Phys. Rev. Lett.* **108**, 214505.

Yakhot, Victor & Sreenivasan, KR 2004 Towards a dynamical theory of multifractals in turbulence. *Physica A: Statistical Mechanics and its Applications* **343**, 147–155.

Appendix A. Numerical simulation

In two–dimensions, by taking curl and divergence of the governing equations 2.1 we obtain two partial differential equations for the two scalars $\omega = \hat{z} \cdot \boldsymbol{\nabla} \times \boldsymbol{u}$ and $\phi = \boldsymbol{\nabla} \cdot \boldsymbol{u}$. We solve these two equations by pseudospectral method. We use the second order Adams–Bashforth method for time evolution of all the terms in the PDEs except the external force, which is integrated by the Euler–Marayuma (Higham 2001) scheme because it is white–in–time.

The velocity field at the off–grid location of the Lagrangian tracers is obtained by using bi-linear interpolation. For the time evolution of the tracers we also use a second order Runge–Kutta scheme.

A.1. *Pseudospectral algoithm for compressible flows*

The use of pseudospectral methods in incompressible turbulence has been long championed by Orszag and others (Canuto *et al.* 2007). They have also been used extensively in DNS of compressible turbulence in both two and three dimensions (Kritsuk *et al.* 2007). A key limitation of the pseudospectral methods for compressible flows is that they are are unable

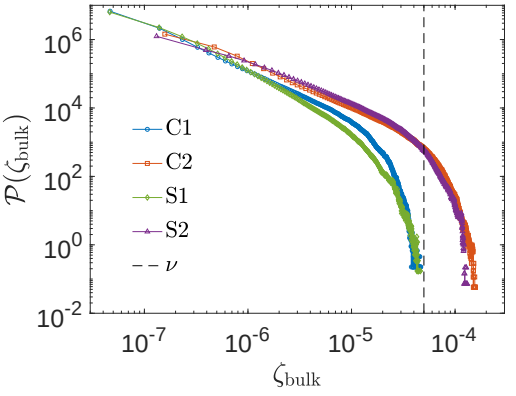

Figure 5: **PDF of the shock viscosity,** $\zeta_{\rm bulk}$, in the NESS of different runs on a log-log scale. While all values of $\zeta_{\rm bulk}$ are less than ν in the low-Mach number runs, C1 and S1, a small fraction (about 1%) of them are higher than ν in the higher-Mach number runs, C2 and S2. These broaden the shocks to a greater extent and enable their resolution at higher Ma.

to capture true discontinuties as opposed to, e.g., Reimann solvers. Shocks in pseudospectral solvers have finite width set by the value of the shock viscosity and this width must be resolved. We discuss the role of shock viscosity in greater detail in section A.2. A further drawback is that they are prone to spurious oscillations near the shocks. We filter out such oscillations by appropriate de-aliasing,see section A.3.

In all cases, the Kolmogorov scale, η, is approximately 6–8 times the grid spacing. Shocks are generally resolved across 4–10 grid points, which is of the order of η.

A.2. *Shock viscosity*

The shock viscosity, $\zeta_{\rm bulk}$, is a spatially non-uniform bulk viscosity which is locally enhanced in the neighbourhood of shocks and serves to resolve the strong shocks on a finite-resolution grid in the high Mach number simulations. We evaluate $\zeta_{\rm bulk}$ on the basis of the prescription outlined in Ref. Von Neumann & Richtmyer (1950). At each grid $(i, j) \equiv \boldsymbol{x}$,

$$\zeta_{\rm bulk}(\boldsymbol{x}) = c_{\rm shock} \left\langle \tilde{\phi} \right\rangle_5 \delta x \delta y \,, \tag{A 1}$$

where $\delta x = \delta y = L/N$ are the grid-spacings along each direction, and $\langle ... \rangle_5$ denotes the average over a 5×5 domain centred at (i, j).

$$\tilde{\phi} = \begin{cases} |\boldsymbol{\nabla} \cdot \boldsymbol{u}| & \text{for} \quad \boldsymbol{\nabla} \cdot \boldsymbol{u} < 0 \,; \\ 0 & \text{otherwise} \,. \end{cases} \tag{A 2}$$

In S1 and C1, we choose $c_{\rm shock} = 1$ while, in S2 and C2, we use $c_{\rm shock} = 5$). Thus, $\zeta_{\rm bulk}$ is non-zero around shocks, decreasing quickly with distance from the latter, and is zero elsewhere. In Fig. 5 we show the PDFs of $\zeta_{\rm bulk}$ for the four runs. We do not consider the locations where $\zeta_{\rm bulk}(\boldsymbol{x}) = 0$, i.e. away from shocks. While $\zeta_{\rm bulk}(\boldsymbol{x}) < \nu$ for all $\boldsymbol{x}$ in the low-Ma runs (C1 and S1), nearly 1% of its values are greater than ν in the higher-Ma flows, C2 and S2.

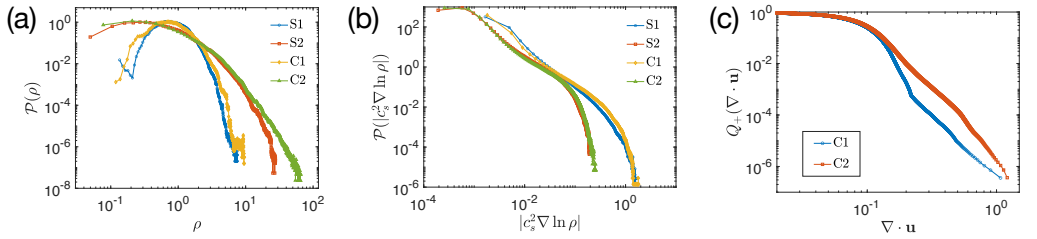

Figure 6: (a) The probability distribution functions (PDFs), $\mathcal{P}(\rho)$, of ρ in the different runs; for a given type of external force, the PDF corresponding to the supersonic flow has broader tails than the transonic one. (b) The PDFs, $\mathcal{P}(|c_s^2\boldsymbol{\nabla}\ln\rho|)$, of the magnitude of the pressure gradient force per unit mass, $|c_s^2\boldsymbol{\nabla}\ln\rho|$, which tends to push tracers away from shocks. The PDFs for the transonic flows have longer tails than the supersonic ones. (c) Complementary cumulative PDFs (CPDFs), $Q_+(\boldsymbol{\nabla}\cdot\boldsymbol{u})$, of the positive velocity divergences in the irrotationally-driven flows, C1 and C2. The supersonic case, C2, has stronger flow divergences, as evidenced from the broader tail of Q_+, than the transonic case, C1.

A.3. *De-aliasing*

To remove aliasing errors, we use an exponential filter (Hou & Li 2007) acting on the nonlinear terms:

$$\mathcal{F}(k) = \exp\left[-36.0\left(\frac{k}{k_{\rm m}}\right)^{36}\right], \tag{A 3}$$

where $k_{\rm m} = N/2$ and N is the number of grid points along either directions. The function, $\mathcal{F}(k)$ is approximately unity up to $k \approx N/3$ and drops quickly but smoothly to almost zero beyond that, hence our aliasing cutoff is approximately $N/3$. We use a smooth filter because it reduces oscillations around the shocks (Hou & Li 2007).

Appendix B. Equal time statistics

The probability distribution functions (PDFs) of the density, ρ, in the NESS of the different runs is shown in Fig. (6a). The PDFs corresponding to the higher-Ma runs (S2 and C2) have broader tails than those of the lower-Ma runs (S1 and C1), indicating a stronger clustering of the tracers in the former. The same may be inferred from Fig. (6b) which displays the PDFs, $\mathcal{P}(|c_s^2\boldsymbol{\nabla}\ln\rho|)$, of the pressure gradient force per unit mass that tends to push the tracers out of the clusters. Among the irrotationally-driven flows, C2 has stronger flow divergences away from shocks than C1, as inferred from the complementary cumulative PDFs, $Q_+(\boldsymbol{\nabla}\cdot\boldsymbol{u})$, of the positive flow divergences in Fig. (6c).

B.1. *Energy spectra*

We display the shell-integrated energy spectra for velocity, $E(k) = |\hat{\boldsymbol{u}}(\boldsymbol{k})|^2$, its solenoidal component, $E_{\rm s}(k) = |\hat{\boldsymbol{u}}^{\rm s}(\boldsymbol{k})|^2$, and its dilational component, $E_{\rm c}(k) = |\hat{\boldsymbol{u}}^{\rm c}(\boldsymbol{k})|^2$, compensated by k^2 in Fig. 7. In all of the cases, we observe $E(k) \sim k^{-2}$ and $E_{\rm c}(k) \sim k^{-2}$ for a decade or more. In the irrotationally-forced runs, $E_{\rm c}(k) \gg E_{\rm s}(k)$ across whole of the inertial range – the difference decreases as Ma increases. $E_{\rm s}(k)$, however, does not appear to have a well-defined power-law regime although it does appear to have a small scaling range with $E_{\rm s}(k) \sim k^{-3}$, marked by a dashed line. .

B.2. *Equal–time structure functions*

We calculate equal-time longitudinal structure functions of the total velocity, $S_{\rm p}(r)$, and its solenoidal, $S_{\rm p}^{\rm s}(r)$, and dilational, $S_{\rm p}^{\rm c}(r)$, see Fig. 8. In each image, the regime of power-law

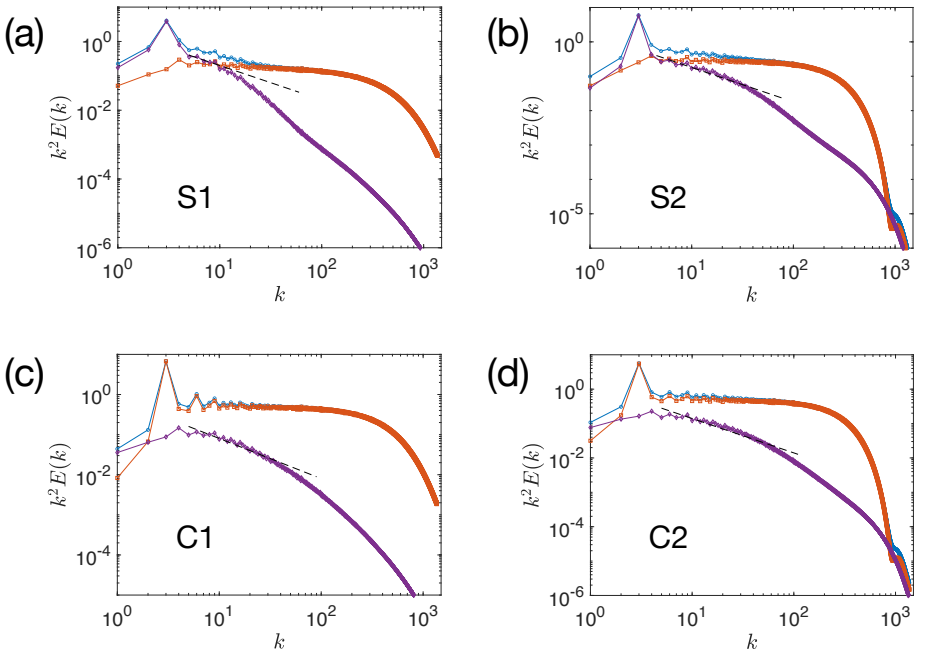

Figure 7: **Velocity spectra.** Log-log plots of the compensated spectra of the total velocity (blue), $E(k) = |\hat{\boldsymbol{u}}(\boldsymbol{k})|^2$, its compressive component (red), $E_c(k) = |\hat{\boldsymbol{u}^{\rm c}}(\boldsymbol{k})|^2$, and its solenoidal components (violet), $E_s(k) = |\hat{\boldsymbol{u}^{\rm s}}(\boldsymbol{k})|^2$, for the different runs; in every image, the dashed line represents k^{-3}; every spectrum has been normalized by $\sum_k E(k)$ in each of the respective runs

fitting has been demarcated by the dashed lines. The scaling regimes of $S_{\rm p}(r)$, $S^{\rm c}_{\rm p}(r)$ and $S^{\rm s}_{\rm p}(r)$ are not exactly identical – there is partial overlap between them and all of them belong to the regime, $\eta \ll r \ll L_{\rm I}$. The fact that, even at a fixed Reynolds number, the scaling range of different quantities are different is found in incompressbile turbulence (Yakhot & Sreenivasan 2004; Schumacher *et al.* 2007) and has also been observed in compressible turbulence Wang *et al.* (2017). We select the range of scales over which we look for scaling of exit times as the range over which $S_{\rm p}(r)$ shows scaling.

To calculate the scaling exponent ζ_p of $S_{\rm p}(r)$ we proceed the following way. We first consider the data from one single snapshot. Identify a scaling range by eye – this range is typically about a decade, but varies from one scheme of forcing to another. Then fit a straight line to the log-log plot of the structure functions to extract ζ_p. We then collect many snapshots into an ensemble. The value of ζ_p we plot in Fig. (9) is the mean over this ensemble and the error is the standard deviation over the same ensemble. In statistical learning theory, this method is called BAGGing or Bootstrap AGGregation (Breiman 1996; Mehta *et al.* 2019). The same method is applied to extract $\zeta^{\rm c}_p$ and $\zeta^{\rm s}_p$. Figure 9 shows that: (a) The solenoidal velocity fluctuations in S1 are less intermittent than those in S2; (b) At large p, ζ_p is much closer to $\zeta^{\rm c}_p$ because $S_{\rm p}(r)$ is dominated by the contribution from the longitudinal velocity differences across shocks which are predominantly irrotational; and (c) The saturation of ζ_p and $\zeta^{\rm c}_p$ at $p \gtrsim 2$ is brought about by the shocks.

Appendix C. Lagrangian averages and dynamic exponents

Our data for the moments of exit–times are averaged over $2n$ uniformly distributed pair separations for a single value of the inital separation R, with $n = 4096^2$. Then the calculations

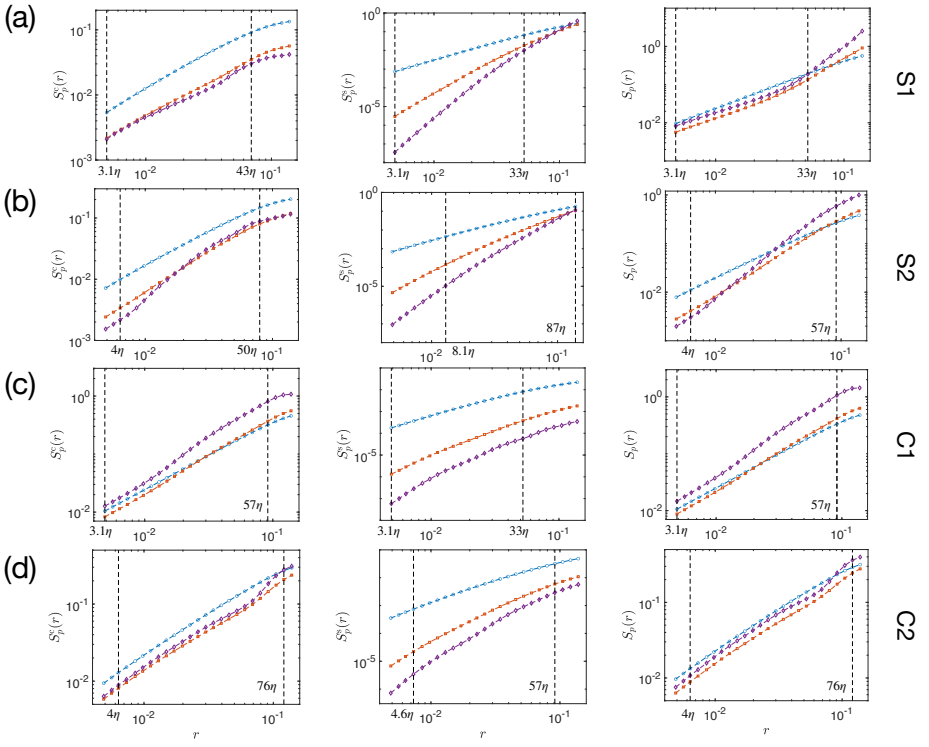

Figure 8: **Equal-time structure functions.** Log-log plots of structure functions: $S_{\rm p}^{\rm c}(r)$ (left column), $S_{\rm p}^{\rm s}(r)$ (middle column) and $S_{\rm p}(r)$ (right column) versus r for $p = 2$ (blue), $p = 4$ (red) and $p = 6$ (violet) in runs (a) S1, (b) S2, (c) C1 and (d) C2. The vertical dashed lines demarcate the region of power-law fitting in each case across which we extract $\zeta_p^{\rm c}$, $\zeta_p^{\rm s}$ and $\zeta_p^{\rm s}$. In each figure, the data has been averaged over a single non-equilibrium steady state (NESS) snapshot.

are repeated for 25 values of R within the inertial range. The log-log plot of the moments of exit times as a function of R are shown in Fig. (10). We run the DNS long enough (close to 3 large–eddy–turnover–time) such that we have more than 10^7 intervals that cross the thresholds for every value of R. This process is repeated for $M = 10$ times by introducing the tracers to M statistically independent initial conditions. Thus for every R we have at least 10^8 samples. We randomly divide our samples into $M = 10$ ensembles and calculate the M individual values of the exponents from each ensemble. The values of the exponents we quote are averaged over the ensemble and the the error we set is the standard deviation of the mean values obtained in each member. In statistical learning theory, this technique is known as BAGGing, or Bootstrap AGGregation (Breiman 1996; Mehta *et al.* 2019). Therefore, from the sizes of the errorbars, we can conclude that the *Lagrangian averages have converged*. To check this further we calculate the exponents from $M/2$ randomly selected members of the ensemble and compare them with the exponents obtained from all (M) the members, see Fig. (11). The excellent overlap between the values of the dynamic exponents in these two cases demonstrate the convergence of the Lagrangian averages.

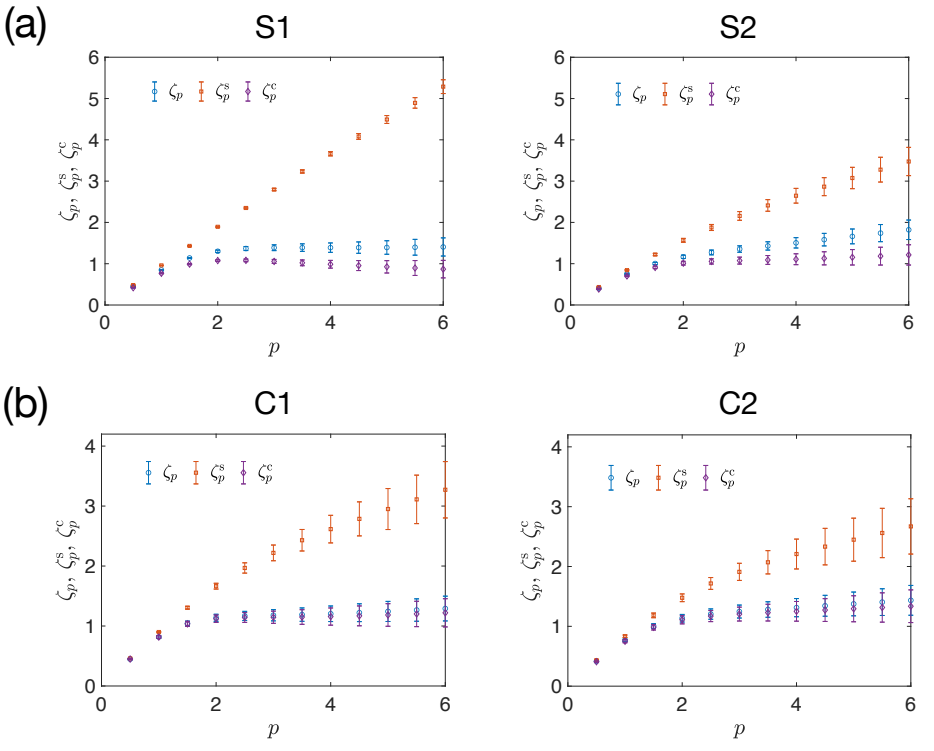

Figure 9: **Equal-time exponents.** Scaling exponents, ζ_p, $\zeta_p^{\rm s}$ and $\zeta_p^{\rm c}$ of the structure functions, $S_{\rm p}(r)$, $S_{\rm p}^{\rm s}(r)$ and $S_{\rm p}^{\rm c}(r)$, of different orders, p.

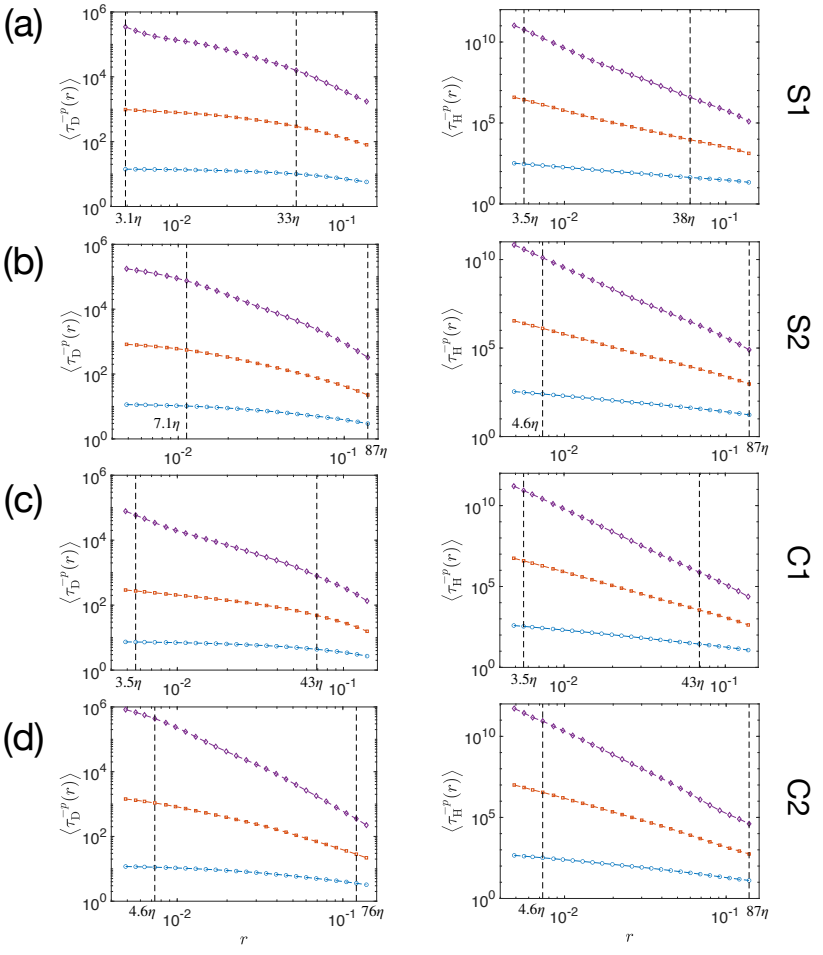

Figure 10: **Moments of Lagrangian exit times.** Log-log plots of $\langle \tau_D^{-p}(R) \rangle$ and $\langle \tau_H^{-p}(R) \rangle$ versus R for $p = 2$ (blue), $p = 4$ (red) and $p = 6$ (violet) in runs (a) S1, (b) S2, (c) C1 and (d) C2. The vertical dashed lines demarkates the region of power–law fitting.

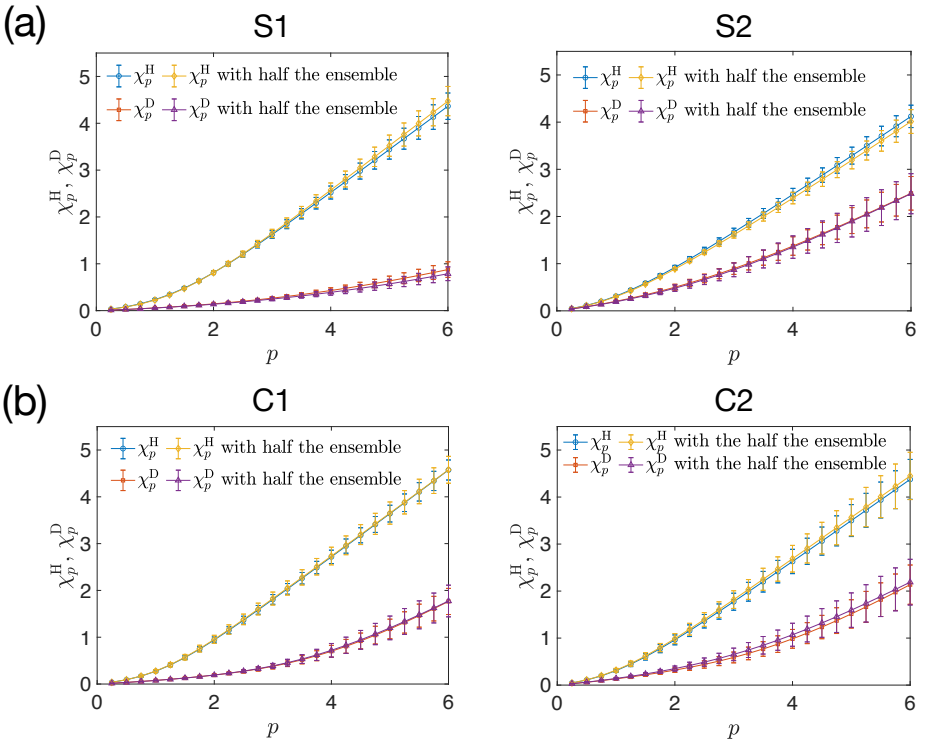

Figure 11: **Convergence of Lagrangian averages.** The dynamic exponents calculated using half (5) the members of the ensemble, compared with the ones calculated using the whole ensemble ($M = 10$), displayed in Fig. 3 of the main text. The excellent overlap between the exponents and their errorbars, in every case affirms the convergence of the Lagrangian averages.